

## █ Ultrahigh-pressure structural changes in a 60 mol. % Al<sub>2</sub>O<sub>3</sub>-40 mol. % SiO<sub>2</sub> glass

I. Ohira, Y. Kono, Y. Shibasaki, C. Kenney-Benson, A. Masuno, G. Shen

### █ Supplementary Information

The Supplementary Information includes:

- Material
- Method
- Figures S-1 to S-5
- Supplementary Information References

### Material

The glass with composition of 60 mol. % Al<sub>2</sub>O<sub>3</sub>-40 mol. % SiO<sub>2</sub> was synthesised from a stoichiometric powder mixture by means of containerless levitation heating method at Hirosaki University, Japan. Blocks of silicate powders (1–2 mg) were levitated in oxygen using an aerodynamic levitator and heated by a 100 W-CO<sub>2</sub> laser. A small vitreous spheroid (~1–2 mm in diameter) was obtained by a cooling rate of a few hundreds of degrees per second. The synthesis of glasses using an aerodynamic levitation furnace is described elsewhere (Rosales-Sosa *et al.*, 2016). The synthesised spheroid was polished to ~150 µm thick of disk and divided into several pieces to put into the sample chamber.

### Method

A double-stage large volume cell, developed in the 200-ton Paris–Edinburgh press at HPCAT of the Advanced Photon Source (Kono *et al.*, 2016, 2018), was used for the high-pressure experiments. The data at ambient pressure was measured without a high-pressure cell. We used a set of cup-shaped WC anvils as the first stage anvils and a set of (100)-oriented single crystal diamonds as the second stage anvils. We used diamond anvils with a 0.6 mm culet beveled to 0.8 mm diameter in experiment 1 and a 0.5 mm culet beveled to 0.7 mm diameter in experiment 2. An aluminum alloy (7075) or beryllium gasket with 150 mm thickness were used as outer gasket for the experiments 1 and 2, respectively. Cubic boron nitride + epoxy (10:1 in weight ratio) was used as the inner gasket inside the metal gasket. The initial sample diameter was 0.23 mm for experiment 1 and 0.20 mm for experiment 2. A piece of gold, used as a pressure marker, was placed at the edge of the glass sample to avoid contamination of the X-ray spectra of gold into that of glass sample. Pressures were determined by using the equation of state of gold (Tsuchiya, 2003). The 220, 311, 222, 400, 331, 420, and 422 reflections of gold were used for calculating the experimental pressures. The X-ray spectra of the gold were collected before and after each structure measurement of the glass sample, except for two pressure points at 4 and 16 GPa where pressure was determined only before or after the structure measurement, respectively. The pressure values are summarised in Table 1



together with the peak positions of  $g(r)$ . Pressure generation as a function of oil load of the Paris–Edinburgh press was shown in Figure S-3. The pressure errors are defined as two-sigma that is calculated from the pressure values determined from the seven reflections measured before and after sample measurements (Table 1). In addition, the pressure difference between the center and the edge of the sample was 8 GPa at the experimental pressure of 108 GPa.

Structure factor,  $S(Q)$ , of the 60 mol. %  $\text{Al}_2\text{O}_3$ –40 mol. %  $\text{SiO}_2$  glass was measured using the multi-angle energy dispersive X-ray diffraction technique (Kono *et al.*, 2014). The incident white X-rays were focused to 0.009 mm (full width at half maximum) in horizontal direction and 0.016 mm in vertical direction in the experiment 1, and to 0.005 mm in horizontal direction and 0.008 mm in vertical direction in the experiment 2 by using a 200-mm-long Pt-coated K-B mirror with an incident angle of 1.25 mrad, which produces an energy cutoff at  $\sim$ 65 keV. We collected series of energy dispersive X-ray diffraction patterns using a Ge solid-state detector (Canberra) at two-theta angles of  $4.6^\circ$ ,  $6.6^\circ$ ,  $8.1^\circ$ ,  $10.6^\circ$ ,  $13.6^\circ$ ,  $17.1^\circ$ ,  $21.1^\circ$ , and  $28.1^\circ$  for the experiment 1,  $3.6^\circ$ ,  $4.6^\circ$ ,  $6.1^\circ$ ,  $8.2^\circ$ ,  $10.7^\circ$ ,  $13.7^\circ$ ,  $17.2^\circ$ ,  $21.2^\circ$ , and  $27.2^\circ$  for the experiment 2, and  $3.1^\circ$ ,  $4.1^\circ$ ,  $5.1^\circ$ ,  $7.1^\circ$ ,  $9.1^\circ$ ,  $12.1^\circ$ ,  $16.1^\circ$ ,  $22.1^\circ$ ,  $28.1^\circ$ , and  $35.1^\circ$  for the ambient pressure measurement. The  $S(Q)$  was determined from the collected energy dispersive X-ray diffraction patterns using the aEDXD program developed by Changyong Park (Kono *et al.*, 2014). Since the minimum  $Q$  range ( $Q_{\min}$ ) is different between the experiments 1 and 2 due to the difference of the lowest two-theta angle in the measurement, we slightly extrapolated the  $S(Q)$  of the experiment 1 from  $1.67 \text{ \AA}^{-1}$  to the  $Q_{\min}$  ( $1.35 \text{ \AA}^{-1}$ ) of the experiment 2 by using a liner extrapolation for consistent analysis of the pair distribution function. A similar extrapolation method has been used in a previous study (Prescher *et al.*, 2017).

The pair distribution function,  $g(r)$ , was calculated by Fourier Transform of  $S(Q)$ :

$$g(r) = 1 + \frac{1}{2\pi^2 n} \int_{Q_{\min}}^{Q_{\max}} Q[S(Q) - 1] \sin(Qr) dQ \quad (\text{Eq. S-1})$$

where  $n$  is the number density. To determine the  $g(r)$  of the A40S glass, we used the second-order polynomial curve of  $\text{SiO}_2$  glass for the data at less than 57.8 GPa ( $\rho = -0.000538 \times P^2 + 0.076284 \times P + 2.203$ ) and the fourth-order Birch–Murnaghan equation of state of the  $\text{SiO}_2$  glass for the data at more than 62.2 GPa ( $\rho_0 = 3.95 \text{ g/cm}^3$ ,  $K_0 = 183.3 \text{ GPa}$ ,  $K_0' = 5.0$ ) (Petitgirard *et al.*, 2017). The Kaplow-type correction using an optimisation procedure (Shen *et al.*, 2003) was applied in determining final structure factors and pair distribution functions. We repeated the optimisation iterations five times. The peak positions in  $g(r)$  were fitted with Gaussian function.

Results of  $g(r)$  and the resultant peak positions of  $g(r)$  ( $r1$ ,  $r2$ , and  $r3$ ) may be influenced by the range of  $Q$  of  $S(Q)$ . In order to evaluate the influence of  $Q$  range on the results of  $g(r)$  and the peak positions, we conducted the analysis of  $g(r)$  at ambient conditions using various  $Q$  ranges (the maximum  $Q$  range,  $Q_{\max} = 10, 11, 12, 13, 14, 15, 16, 17 \text{ \AA}^{-1}$ ). The results are shown in Supplementary Figures (Figs. S-4 and S-5). The peak positions of  $g(r)$  are similar when  $Q_{\max}$  are higher than  $12 \text{ \AA}^{-1}$ , while the  $r1$ – $r3$  become scattered when  $Q_{\max}$  are less than  $\sim 11 \text{ \AA}^{-1}$ . These data clearly show that our analysis with the  $Q_{\max} = 14 \text{ \AA}^{-1}$  is of high enough quality to determine the peak positions of the  $g(r)$ . We defined the errors of the  $r1$ – $r3$  at ambient conditions as a square-root of sum of squares of  $3\sigma$  of the peak positions of the analyses using the  $Q_{\max}$  of  $12$ – $17 \text{ \AA}^{-1}$  and  $3\sigma$  of peak-fitting errors (Table 1). The same procedure was applied to high pressure data with the  $Q_{\max}$  of  $10, 11, 12, 13, 14 \text{ \AA}^{-1}$  (Fig. S-5). At high  $Q_{\max}$  between  $11$  and  $14 \text{ \AA}^{-1}$ ,  $r1$  and  $r3$  values are within the error bar, although the  $r2$  shows slightly higher value at  $Q_{\max} = 11$ . At  $Q_{\max} = 10 \text{ \AA}^{-1}$ , all the  $r1$ – $r3$  show deviation from those obtained at the  $Q_{\max}$  higher than  $11$ . With consideration of these uncertainties, the fluctuation of the  $r1$ – $r3$  in the analysis of  $Q_{\max} = 11, 12, 13, 14 \text{ \AA}^{-1}$  are adopted as the errors of the  $r1$ – $r3$  due to  $Q_{\max}$ . The largest  $3\sigma$  of each peak position at the  $Q_{\max}$  of  $11$ – $14 \text{ \AA}^{-1}$  is  $0.006 \text{ \AA}^\circ$  for  $r1$ ,  $0.039 \text{ \AA}^\circ$  for  $r2$ , and  $0.040 \text{ \AA}^\circ$  for  $r3$ , and we adopted it as the error due to  $Q_{\max}$  in all high pressure measurement. Then, we calculated square-root of sum of squares of the  $3\sigma$  due to  $Q_{\max}$  and the  $3\sigma$  of peak-fitting, as the errors of  $r1$ – $r3$  at high pressure conditions (Table 1).



## Supplementary Figures

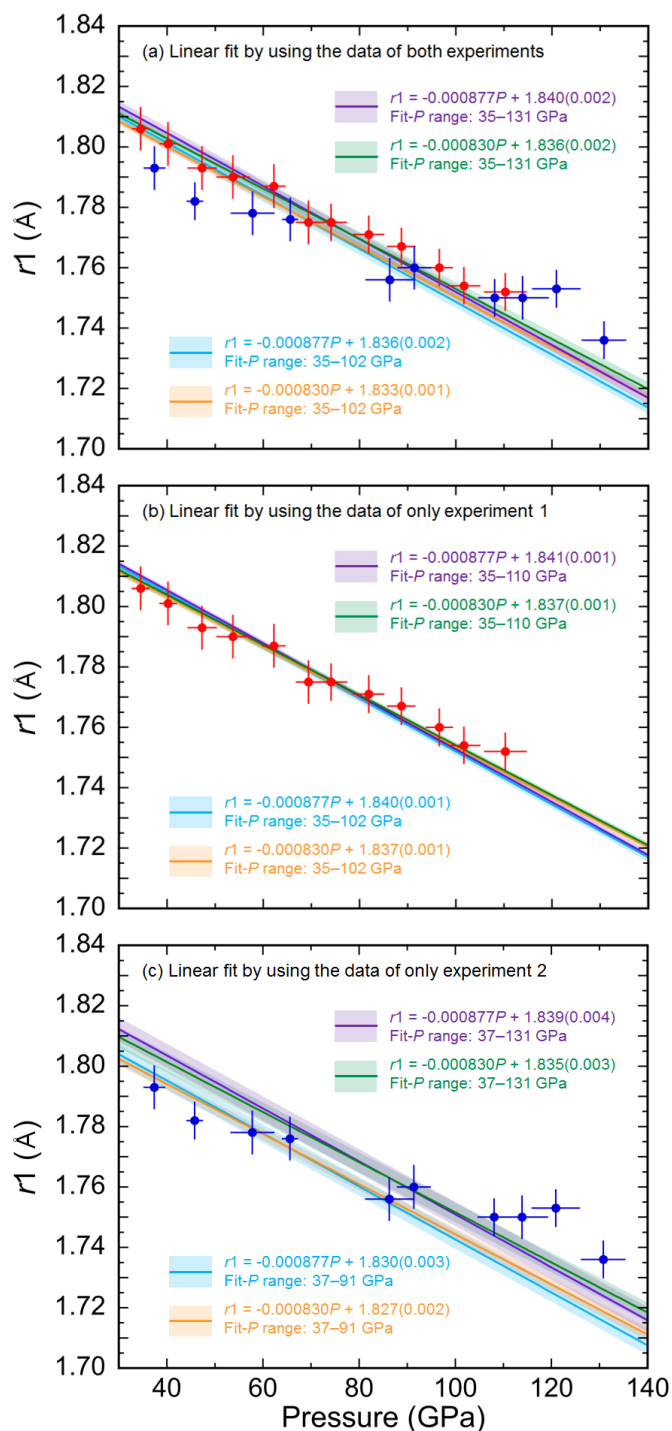


**Figure S-1** The first ( $r_1$ ) peak position of  $g(r)$  of the A40S glass with the fitting lines. Red and blue circles indicate the  $r_1$  determined in the high-pressure experiments 1 and 2, respectively. **(a)** Linear fit for  $r_1$  obtained from both of the two experiments. The light blue and orange lines are obtained from fitting for the  $r_1$  of A40S glass at 35–102 GPa, using the  $dr_1/dP$  values of the Si–O and Al–O bond distances with CN of 6 ( $-8.77 \times 10^{-4}$  Å/GPa, Sato and Funamori, 2010;  $-8.30 \times 10^{-4}$  Å/GPa, Ghosh and Karki, 2018, respectively), as same as the Figure 2a. The purple and green lines are obtained from fitting at 35–131 GPa using the same  $dr_1/dP$  values. **(b)** Linear fit for  $r_1$  obtained from only the experiment 1. Two fitting ranges (35–102 GPa and 35–110 GPa) were applied using the  $dr_1/dP$  values same as (a). **(c)** Linear fit for  $r_1$  obtained from only the experiment 2. Two fitting ranges (37–91 GPa and 37–131 GPa) were applied using the  $dr_1/dP$  values same as (a). The shaded bands surrounding the lines indicate the fitting errors. When the data up to 131 GPa are fit, the fitting lines show slightly higher values than those determined by using the data up to 102 GPa. Nevertheless, the  $r_1$  above 110 GPa shows deviation from the fitting lines. In addition, since there is somewhat difference in the  $r_1$  of up to 0.013 Å between the two experiments, we evaluated the linear fit in each experiment. Even if the plot for the  $r_1$  is fit in the experiment 1 and 2, individually (b, c), the deviation of the  $r_1$  above 110 GPa can also be clearly identified.



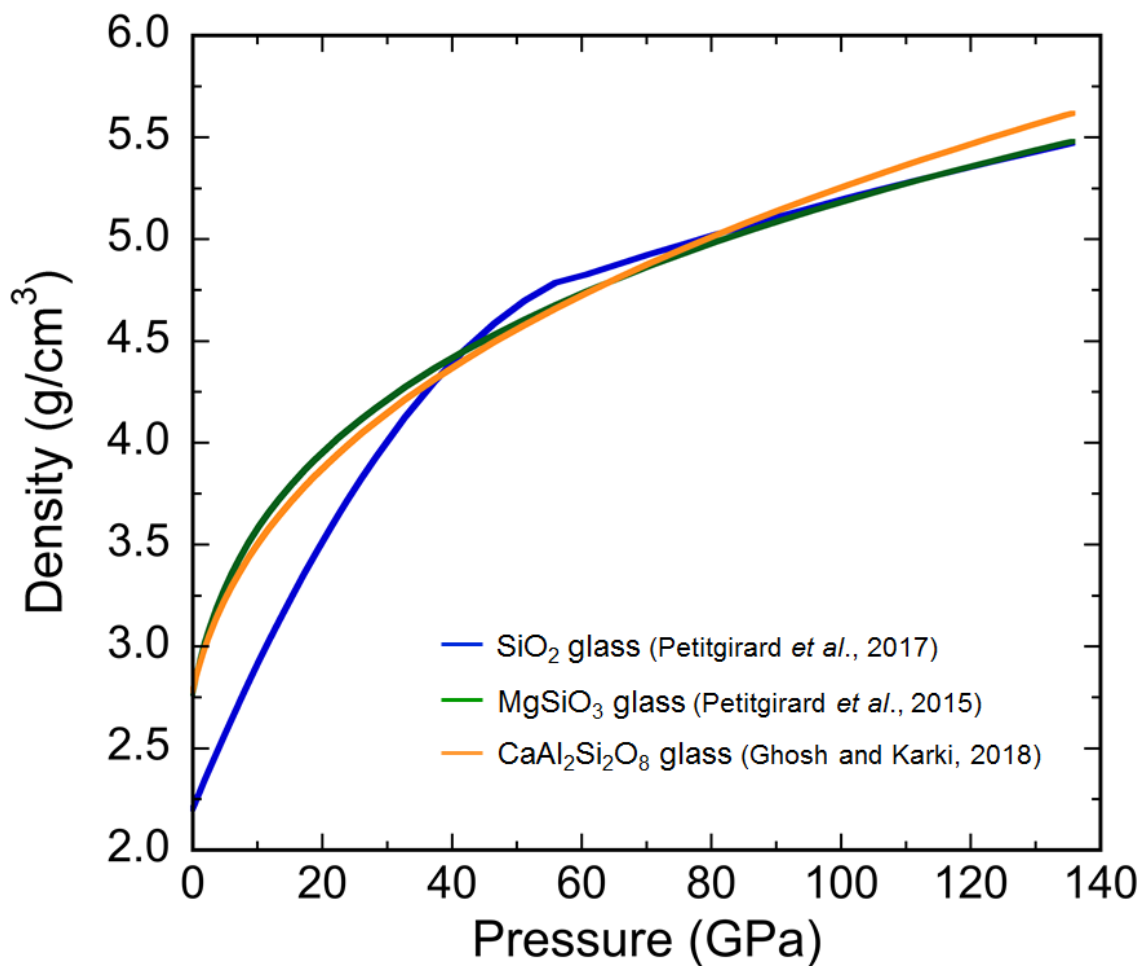


**Figure S-2** Density of  $\text{SiO}_2$  (blue: Petitgirard *et al.*, 2017),  $\text{MgSiO}_3$  (green: Petitgirard *et al.*, 2015), and  $\text{CaAl}_2\text{Si}_2\text{O}_8$  (orange: Ghosh and Karki, 2018) glasses reported in the previous studies.



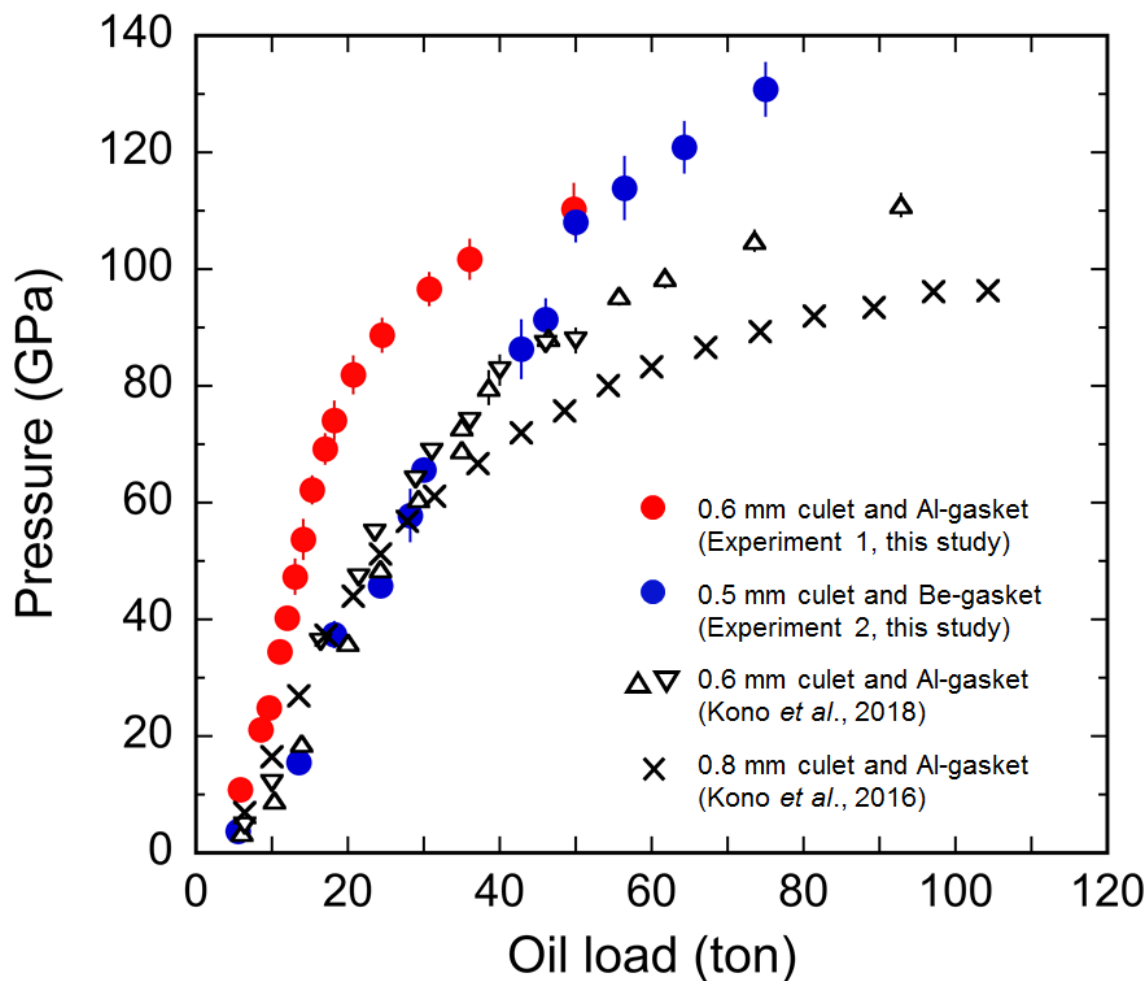


**Figure S-3** Pressure generation as a function of oil load of the large volume press. Red (experiment 1) and blue (experiment 2) solid circles represent pressure conditions of the structure measurements in this study. Black symbols represent pressure generation of the previous studies (Kono *et al.*, 2016, 2018).



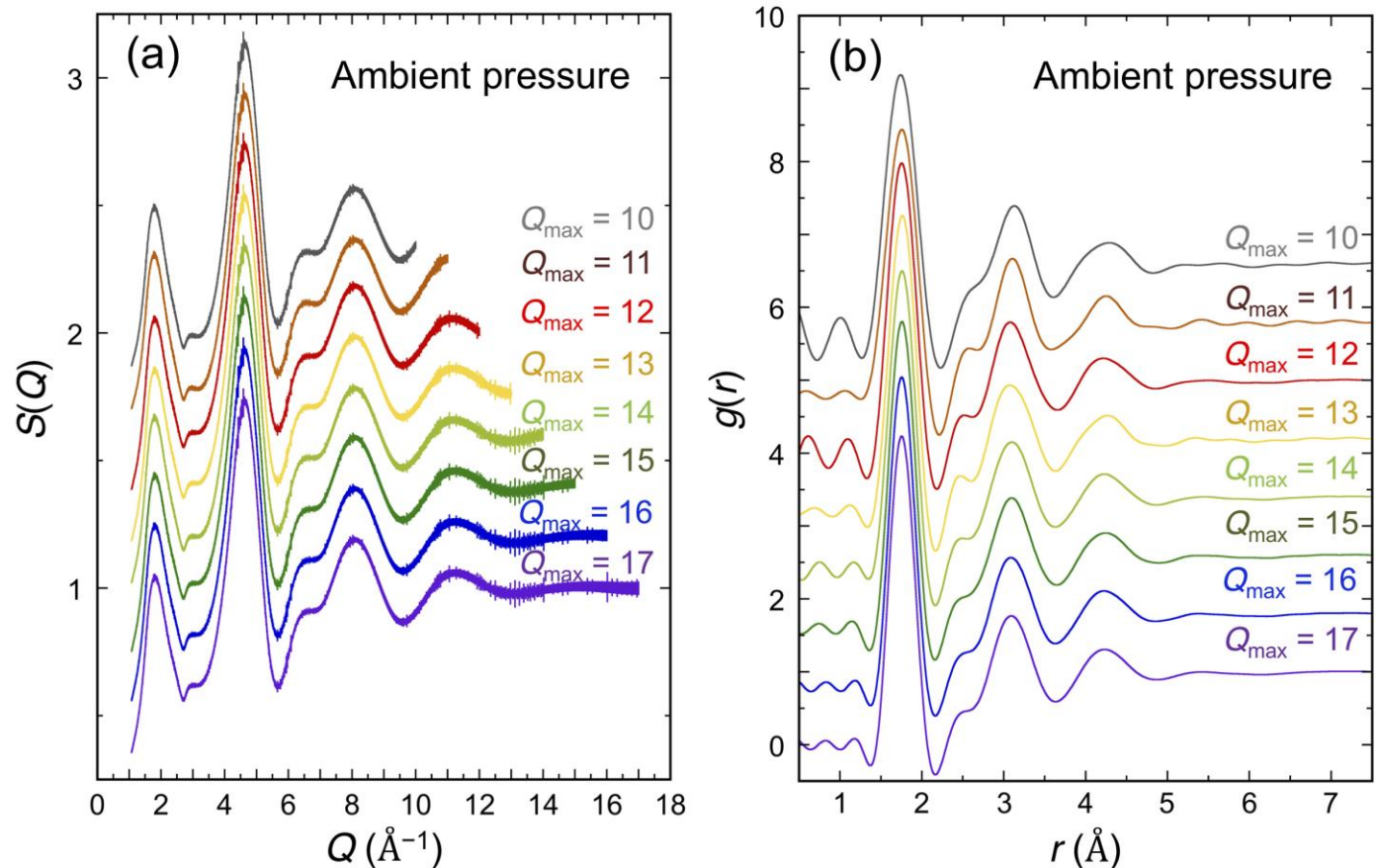


**Figure S-4** Results of (a)  $S(Q)$  and (b)  $g(r)$  of A40S glass analysed by using different  $Q_{\max}$  at ambient condition. (a)  $S(Q)$  are displayed by a vertical offset of 0.2. (b)  $g(r)$  are displayed by vertical offset of 0.8.



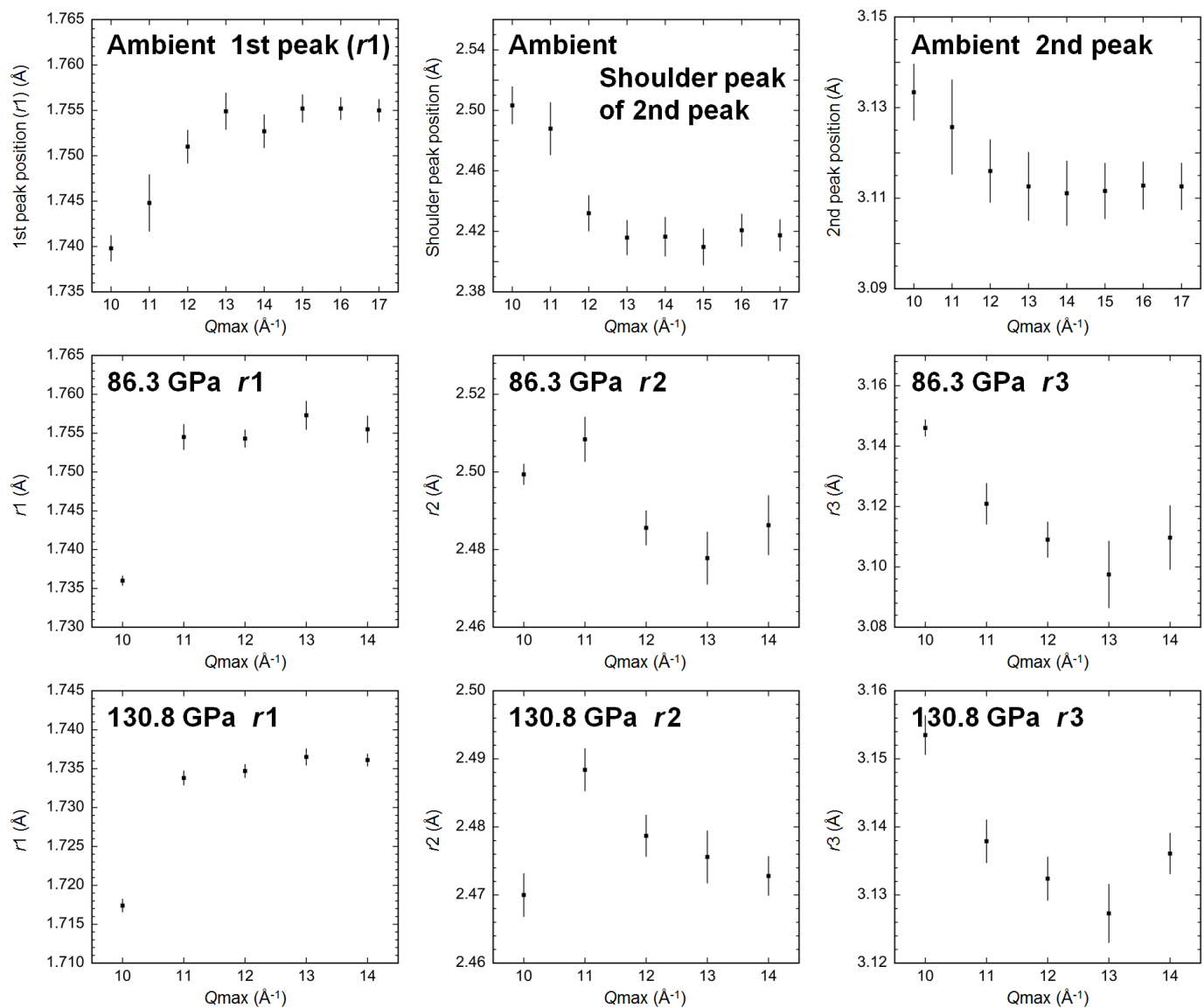


**Figure S-5** Variation of the peak positions as a function of  $Q_{\text{max}}$  evaluated at ambient conditions, 86.3 GPa, and 130.8 GPa. The error bars indicate  $3\sigma$  of peak fitting error.



## Supplementary Information References

- Ghosh, D.B., Karki, B.B. (2018) First-principles molecular dynamics simulations of anorthite ( $\text{CaAl}_2\text{Si}_2\text{O}_8$ ) glass at high pressure. *Physics and Chemistry of Minerals* 45, 575–587.
- Kono, Y., Park, C., Kenney-Benson, C., Shen, G., Wang, Y. (2014) Toward comprehensive studies of liquids at high pressures and high temperatures: Combined structure, elastic wave velocity, and viscosity measurements in the Paris–Edinburgh cell. *Physics of the Earth and Planetary Interiors* 228, 269–280.
- Kono, Y., Kenney-Benson, C., Ikuta, D., Shibasaki, Y., Wang, Y., Shen, G. (2016) Ultrahigh-pressure polyamorphism in  $\text{GeO}_2$  glass with coordination number >6. *Proceedings of the National Academy of Sciences of the United States of America* 113, 3436–3441.
- Kono, Y., Shibasaki, Y., Kenney-Benson, C., Wang, Y., Shen, G. (2018) Pressure-induced structural change in  $\text{MgSiO}_3$  glass at pressures near the Earth's core–mantle boundary. *Proceedings of the National Academy of Sciences of the United States of America* 115, 1742–1747.
- Petitgirard, S., Malfait, W.J., Simmyo, R., Kupenko, I., Hennet, L., Harries, D., Dane, T., Burghammer, M., Rubie, D.C. (2015) Fate of  $\text{MgSiO}_3$  melts at core–mantle boundary conditions. *Proceedings of the National Academy of Sciences of the United States of America* 112, 14186–14190.
- Petitgirard, S., Malfait, W.J., Journaux, B., Collings, I.E., Jennings, E.S., Blanchard, I., Kantor, I., Kurnosov, A., Cotte, M., Dane, T., Burghammer, M., Rubie, D.C. (2017)  $\text{SiO}_2$  glass density to lower-mantle pressures. *Physical Review Letters* 119, 215701.
- Rosales-Sosa, G.A., Masuno, A., Higo, Y., Inoue, H. (2016) Crack-resistant  $\text{Al}_2\text{O}_3$ – $\text{SiO}_2$  glasses. *Scientific Reports* 6, 23620.
- Prescher, C., Prakapenka, V.B., Stefanski, J., Jahn, S., Skinner, L.B., Wang, Y. (2017) Beyond sixfold coordinated Si in  $\text{SiO}_2$  glass at ultrahigh pressures. *Proceedings of the National Academy of Sciences of the United States of America* 114, 10041–10046.
- Sato, T., Funamori, N. (2010) High-pressure structural transformation of  $\text{SiO}_2$  glass up to 100 GPa. *Physical Review B* 82, 184102.
- Shen, G., Prakapenka, V.B., Rivers, M.L., Sutton, S.R. (2003) Structural investigation of amorphous materials at high pressures using the diamond anvil cell. *Review of Scientific Instruments* 74, 3021–3026.
- Tsuchiya, T. (2003) First-principles prediction of the  $P$ - $V$ - $T$  equation of state of gold and the 660-km discontinuity in Earth's mantle. *Journal of Geophysical Research* 108, 2462.

